Deep Learning Accelerated Brain Diffusion-Weighted MRI with Super Resolution Processing

Sebastian Altmann, MD[1], Nils F. Grauhan, MD[1], Mario Alberto Abello Mercado, MD, Sebastian Steinmetz, Andrea Kronfeld, PhD, Roman Paul, MSc, Thomas Benkert, PhD, Timo Uphaus, MD, Sergiu Groppa, MD, Yaroslav Winter, MD, Marc A. Brockmann, MD, Ahmed E. Othman, MD

Objectives: To investigate the clinical feasibility and image quality of accelerated brain diffusion-weighted imaging (DWI) with deep learning image reconstruction and super resolution.

Methods: 85 consecutive patients with clinically indicated MRI at a 3 T scanner were prospectively included. Conventional diffusion-weighted data (c-DWI) with four averages were obtained. Reconstructions of one and two averages, as well as deep learning diffusion-weighted imaging (DL-DWI), were accomplished. Three experienced readers evaluated the acquired data using a 5-point Likert scale regarding overall image quality, overall contrast, diagnostic confidence, occurrence of artefacts and evaluation of the central region, basal ganglia, brainstem, and cerebellum. To assess interrater agreement, Fleiss' kappa ($\varkappa$) was determined. Signal intensity (SI) levels for basal ganglia and the central region were estimated via automated segmentation, and SI values of detected pathologies were measured.

Results: Intracranial pathologies were identified in 35 patients. DL-DWI was significantly superior for all defined parameters, independently from applied averages (p-value < 0.001). Optimum image quality was achieved with DL-DWI by utilizing a single average (p-value < 0.001), demonstrating very good (80.9%) to excellent image quality (14.5%) in nearly all cases, compared to 12.5% with very good and 0% with excellent image quality for c-MRI (p-value < 0.001). Comparable results could be shown for diagnostic confidence. Inter-rater Fleiss' Kappa demonstrated moderate to substantial agreement for virtually all defined parameters, with good accordance, particularly for the assessment of pathologies (p = 0.74). Regarding SI values, no significant difference was found.

Conclusion: Ultra-fast diffusion-weighted imaging with super resolution is feasible, resulting in highly accelerated brain imaging while increasing diagnostic image quality.

Key Words: Deep learning acceleration; Diffusion-weighted brain MRI; Super resolution; Image quality; Accelerated brain imaging.

INTRODUCTION

Diffusion-weighted imaging (DWI) is of great importance, especially in neuroimaging, where it has become an indispensable method to detect acute ischemia, radiation necrosis, infectious diseases, and to differentiate between various neoplastic lesions (1–3). As it highlights differences in water diffusion before the net increase of water content in the subacute phase of the infarct, changes in DWI and the Apparent Diffusion Coefficient (ADC) values can be detected within minutes from the onset of ischemia (4,5). Moreover, when dealing with acute ischemia, DWI/ Fluid-attenuated inversion recovery (FLAIR) mismatch has a high specificity and positive predictive value in identifying patients with remaining penumbra, who may benefit from mechanical thrombectomy (6).

Single-shot echo planar imaging (SS-EPI) is commonly used for DWI acquisitions. Unfortunately, corresponding

Acad Radiol 2024; 31:4171–4182

From the Department of Neuroradiology, University Medical Center Mainz, Johannes Gutenberg University, Langenbeckstr. 1, 55131 Mainz, Germany (S.A., N.F.G., M.A.A.M., S.S., A.K., M.A.B., A.E.O.); Institute of Medical Biostatistics, Epidemiology and Informatics (IMBEI), University Medical Center Mainz, Johannes Gutenberg University, Rhabanusstr. 3/Tower A, 55118 Mainz, Germany (R.P.); Siemens Healthineers AG, Erlangen, Germany (T.B.); Department of Neurology, University Medical Center Mainz, Johannes Gutenberg University, Langenbeckstr. 1, 55131 Mainz, Germany (T.U., S.G., Y.W.); Department of Neurology, Philipps-University Marburg, Baldingerstr, 35043 Marburg, Germany (Y.W.). Received December 31, 2023; revised February 20, 2024; accepted February 26, 2024. **Address correspondence to**: S.A. e-mail: Sebastian.altmann@unimedizin-mainz.de

[1] Sebastian Altmann and Nils F Grauhan contributed equally to this publication.

https://doi.org/10.1016/j.acra.2024.02.049

images often suffer from distortion and blurring due to the limited bandwidth along the phase encoding direction. As a result, their diagnostic value can be limited. In order to resolve these problems, various methods have been developed, including field mapping (7–9). Furthermore, integrating readout segmentation EPI techniques such as readout segmentation of long variable echo trains (RESOLVE) effectively mitigate susceptibility-based distortion of DWI, surpassing the limitations of the single-shot EPI technique (10). Notably, these techniques require longer scanning times and are more susceptible to motion interference. As a result, they are typically utilized to study small areas in close proximity to air-tissue interfaces (11).

In recent years, deep learning-based (DL) image reconstruction in MRI has been increasingly applied due to its ability to facilitate faster image acquisition while preserving the required diagnostic image quality (12–14). Furthermore, DL-based super resolution processing can enhance the spatial resolution of conventional DWI (c-DWI) sequences (15,16).

We hypothesized that DL-reconstruction in combination with super resolution is clinically feasible, generating high-quality diagnostic images while reducing the number of required averages thus resulting in a reduction of acquisition time. Therefore, our study aimed to validate a novel DL-enhanced diffusion-weighted imaging sequence (DL-DWI), which combines DL-based image reconstruction with super resolution processing for SS-EPI.

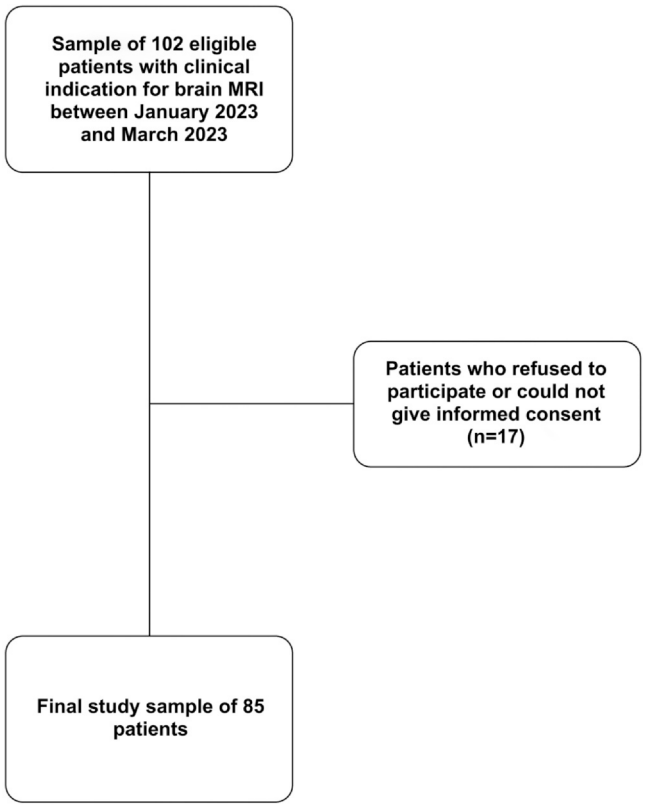

Figure 1. Flow diagram of study inclusion and exclusion criteria.

MATERIALS AND METHODS

Study Sample

This single-center prospective study was approved by our institution's local ethics committee, and written informed consent was obtained (approval number: 2021–15811). Our study was conducted in accordance with the Declaration of Helsinki and its amendments.

Among 102 eligible patients, 85 consecutive patients were included in this study, receiving a clinically indicated brain MRI between January 2023 and March 2023 (Fig 1). Inclusion criteria were: i) age > 18 years, ii) clinically stable patients (spontaneously breathing, not intubated, stable vital signs), iii) ability to give informed consent. Patients were excluded in case of any MRI contraindication.

Image Acquisition

All measurements were performed on a 3 T clinical scanner (MAGNETOM Skyra, Siemens Healthineers, Erlangen, Germany) with a 64-channel head and neck coil. Conventional diffusion-weighted data were obtained after the patients' clinically indicated examination. These data were reconstructed with conventional GRAPPA to get the standard DWI images (b0/b1000; four averages; 119 s). By retrospectively reducing the number of averages, abbreviated acquisitions were simulated, and DL-based images were reconstructed with a research application software (b0/b1000; two averages; 73 s and one average 50 s). The relevant sequence parameters of the study sequences are listed in Table S1.

Deep Learning Reconstruction

DL-DWI employed a deep learning-based reconstruction scheme consisting of two subsequent steps: I) As the first step, k-space to image reconstruction following the idea of a variational network (17) was conducted using precalculated coil sensitivities as well as acquired single-shot k-space data. In total, 17 unrolled iterations were performed with Nesterov extrapolation and trainable step sizes (18). The initial six iterations applied data consistency without additional regularization to focus on parallel imaging, i.e. to fill missing k-space information. To focus on denoising, the following 11

iterations additionally employed convolutional neural network-based regularization with hierarchical down-up architecture. With the corresponding image-to-image neural network, feature maps are extracted from the complex input images by iteratively down-sampling with U-blocks using convolutions with stride 2, before up-sampling them with subpixel convolutions. The training was performed using a complex L1 loss function on about 500.000 single-shot DWI images. To ensure applicability of the method in real-word scenarios and generalization across different field strengths and scanner types, these images have been collected on various clinical 1.5 T and 3 T scanners (MAGNETOM, Siemens Healthineers, Erlangen, Germany) and included different body regions. Only the k-space data were stored and accessed for training purposes which did not contain any patient-specific information. The acceleration factor was retrospectively doubled to generate training pairs. II) In the second step, the DL-based reconstructed single-shot images were further processed using an image-based super resolution network to increase spatial resolution. A pixel shuffle network (19) was trained on volunteer images from different sequences and various body regions. From these data, low-resolution images were generated by down-sampling spatial resolution by a factor of two, both along the readout and phase-encoding direction. The corresponding image pairs served as input for the training. Only the undersampled parts of k-space were extrapolated by applying hard data consistency to ensure that the acquired image content was not modified.

Both reconstruction algorithms were trained offline in a supervised setting using PyTorch. After training, the networks were frozen and integrated into the C++ based reconstruction pipeline at the scanner. After these two reconstruction steps, DWI-specific steps such as averaging (by building the arithmetic mean), trace-weighting (by building the geometric mean), and ADC calculation (by log-linear fitting) were performed

TABLE 1. Patient Characteristics

Characteristics	Value ($n = 85$)
Age (years)*	55.1 ± 17.1 (22–94)
Median age	54.0
Sex	
Male	36 (42.4%)
Female	49 (57.6%)
Pathologic findings	35 (41.2%)
Metastasis	11 (12.9%)
Acute/subacute infarction	7 (8.2%)
Chronic infarction	4 (4.7%)
Acute/subacute demyelinization	3 (3.5%)
Intracranial hemorrhage	2 (2.4%)
Neuroglial neoplasia	2 (2.4%)
Severe periventricular Gliosis	1 (1.1%)
Postoperative scar	1 (1.1%)
Hygroma	1 (1.1%)
Cavernoma	1 (1.1%)
Ventriculitis	1 (1.1%)
Large postoperative Defect	1 (1.1%)
No clinically relevant findings	50 (58.8%)

* Data are mean ± 1 SD, with ranges in parentheses

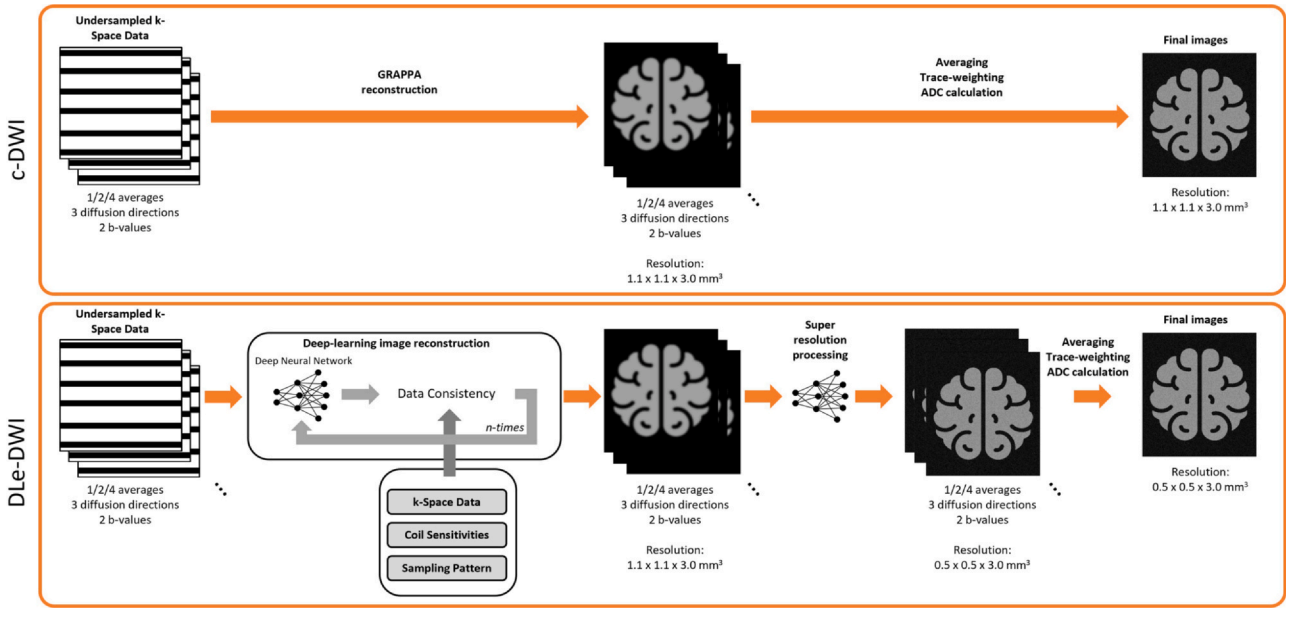

Figure 2. Schematic of the reconstruction pipeline used for c-DWI and DLe-DWI. C-DWI, conventional diffusion-weighted imaging; DL-DWI, deep learning-based diffusion-weighted imaging.

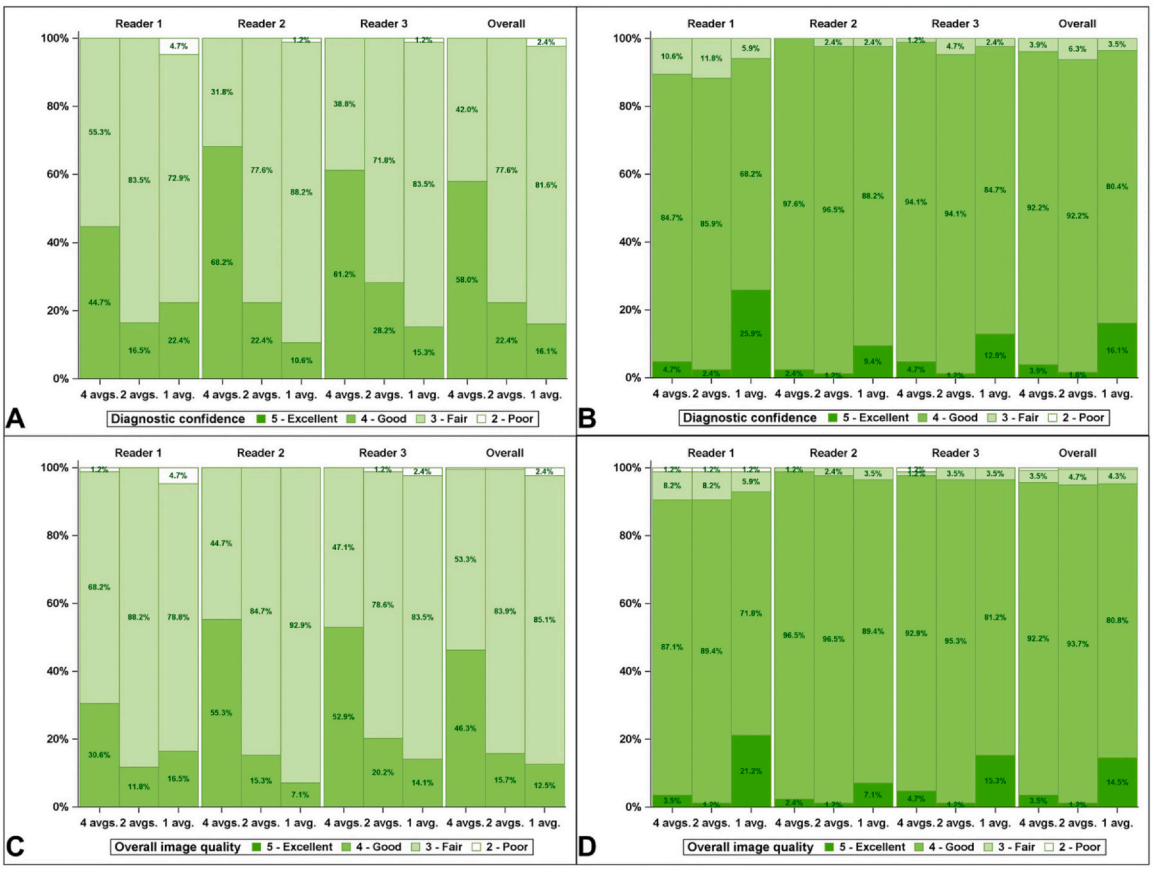

Figure 3. Results of the analysis of overall image quality and diagnostic confidence for conventional and deep learning accelerated sequences; c-DWI (A + C), DL-DWI (B + D). C-DWI, conventional diffusion-weighted imaging; DL-DWI, deep learning-based diffusion-weighted imaging.

identically to standard DWI. In DL-based reconstruction methods, the computationally demanding task is the training process of the networks, while the actual inference requires significantly less time. Given that the training was performed once and in an offline setting, only the inference time is decisive for the clinical workflow. The inference time for each DL-DWI dataset was less than 2 min, therefore not limiting the clinical applicability of the proposed reconstruction. The described DL-based reconstruction steps were performed without sharing information between different b-values, diffusion directions, or averages. This enabled the retrospective reduction of averages, used in this study to simulate accelerated scans by only applying the reconstruction on a subset of the originally acquired averages. A schematic of the reconstruction pipeline is depicted in Figure 2.

Subjective Image Evaluation

Subjective image evaluation was performed by three radiologists (___ with five years of experience in brain MRI; ___ and ___ with seven years of experience in brain MRI), blinded to the imaging protocols. Any participant- or sequence-identifying markers were removed. The raters assessed subjective image quality regarding overall image quality, the occurrence of artefacts, and diagnostic confidence. Furthermore, an assessment of several anatomic regions (central region, basal ganglia, cerebellum) and assessment of pathologies was performed. The raters used a 5-point Likert scale throughout all patients and categories, as shown in Table S2.

(Semi-)Quantitative Image Analysis

The automated determination of the mean diffusion parameters (TRACE and ADC) of the white matter and basal ganglia was performed using SPM 12 (The Welcome Centre for Human Neuroimaging, UCL Queen Square Institute of Neurology, London, UK) and Matlab 2022b (The MathWorks, Natick/MA, USA). Diffusion-weighted datasets were first coregistered to a T1-weighted volume dataset

TABLE 2. Odds Ratios for Different Averages and Different Techniques

	c-DWI								
	DL-DWI	1 Avg.			2 Avg.			4 Avg.		
Parameter	Avg.	OR	CI	p	OR	CI	p	OR	CI	p
Artefacts	1	1.13	0.93; 1.38	0.209	1.11	0.92; 1.34	0.254	0.96	0.80; 1.15	0.657
	2	1.14	0.91; 1.41	0.250	1.12	0.93; 1.34	0.225	0.96	0.80; 1.15	0.672
	4	1.16	0.93; 1.44	0.177	1.14	0.95; 1.38	0.166	0.98	0.84; 1.15	0.824
Basal Ganglia	1	820.09	369.06;1822.34	**< 0.001**	313.03	146.80; 667.52	**< 0.001**	86.08	41.74; 177.53	**< 0.001**
	2	160.89	84.28; 307.16	**< 0.001**	61.41	35.43; 106.46	**< 0.001**	16.89	10.20; 27.97	**< 0.001**
	4	230.93	111.08; 480.09	**< 0.001**	88.15	46.98; 165.38	**< 0.001**	24.24	13.75; 42.74	**< 0.001**
Central Region	1	585.12	286.73;1194.03	**< 0.001**	213.75	110.56; 413.27	**< 0.001**	69.56	36.69; 131.91	**< 0.001**
	2	72.65	42.34; 124.64	**< 0.001**	26.54	17.15; 41.08	**< 0.001**	8.64	5.76; 12.95	**< 0.001**
	4	128.30	64.93; 253.52	**< 0.001**	46.87	27.05; 81.22	**< 0.001**	15.25	8.95; 25.99	**< 0.001**
Cerebellum	1	47.68	28.71; 79.19	**< 0.001**	23.89	14.78; 38.63	**< 0.001**	11.39	7.33; 17.68	**< 0.001**
	2	25.41	16.72; 38.62	**< 0.001**	12.73	8.92; 18.17	**< 0.001**	6.07	4.34; 8.48	**< 0.001**
	4	21.88	13.93; 34.37	**< 0.001**	10.96	7.72; 15.57	**< 0.001**	5.23	3.76; 7.26	**< 0.001**
Diagnostic Confidence	1	412.41	175.18; 970.89	**< 0.001**	247.96	108.62; 566.05	**< 0.001**	53.68	23.69; 121.61	**< 0.001**
	2	70.05	39.15; 125.33	**< 0.001**	42.12	24.97; 71.02	**< 0.001**	9.12	5.74;14.48	**< 0.001**
	4	118.06	60.88; 228.94	**< 0.001**	70.98	38.31; 131.53	**< 0.001**	15.37	8.79; 26.87	**< 0.001**
Brainstem	1	29.82	19.23; 46.25	**< 0.001**	18.37	12.44; 27.13	**< 0.001**	8.88	6.35; 12.41	**< 0.001**
	2	28.77	18.26; 45.35	**< 0.001**	17.73	12.37; 25.41	**< 0.001**	8.57	6.10; 12.03	**< 0.001**
	4	21.18	13.50; 33.21	**< 0.001**	13.05	8.99; 18.94	**< 0.001**	6.30	4.56; 8.72	**< 0.001**
Overall Image Quality	1	389.94	161.55; 941.24	**< 0.001**	277.41	116.34; 661.46	**< 0.001**	65.68	28.95; 149.01	**< 0.001**
	2	92.45	49.44; 172.88	**< 0.001**	65.77	36.51; 118.48	**< 0.001**	15.57	9.62; 25.20	**< 0.001**
Assessment of Pathologies	1	471.26	172.17;1289.94	**< 0.001**	109.49	50.06; 239.51	**< 0.001**	33.90	15.23; 75.42	**< 0.001**
	2	139.99	57.33; 341.81	**< 0.001**	32.53	16.82; 62.91	**< 0.001**	10.07	5.48; 18.49	**< 0.001**
	4	170.34	66.82; 434.21	**< 0.001**	39.58	19.22; 81.51	**< 0.001**	12.25	6.29; 23.87	**< 0.001**

Avg., averages; c-DWI, conventional diffusion-weighted imaging; CI, Confidence interval; DL-DWI, deep learning-based diffusion-weighted imaging; OR, Odds ratio

TABLE 3. Results of Multi-reader Inter-rater Agreement for DWI

Parameter	Avg.	c-DWI		DL-DWI	
	κ_m	95%-CI	κ_m	95%-CI	
Artefacts	1 avg.	0.80	[0.722;0.882]	0.78	[0.691;0.869]
	2 avgs.	0.78	[0.693;0.869]	0.77	[0.674;0.858]
	4 avgs.	0.86	[0.793;0.932]	0.80	[0.72;0.888]
Basal Ganglia	1 avg.	0.52	[0.362;0.675]	0.52	[0.4;0.649]
	2 avgs.	0.56	[0.392;0.73]	0.40	[0.114;0.686]
	4 avgs.	0.51	[0.378;0.648]	0.53	[0.337;0.721]
Central Region	1 avg.	0.57	[0.443;0.687]	0.65	[0.558;0.748]
	2 avgs.	0.50	[0.352;0.656]	0.35	[0.075;0.615]
	4 avgs.	0.52	[0.39;0.657]	0.47	[0.285;0.648]
Cerebellum	1 avg.	0.53	[0.395;0.664]	0.64	[0.503;0.78]
	2 avgs.	0.74	[0.623;0.866]	0.51	[0.303;0.727]
	4 avgs.	0.72	[0.596;0.835]	0.44	[0.236;0.642]
Diagnostic Confidence	1 avg.	0.53	[0.382;0.67]	0.50	[0.311;0.689]
	2 avgs.	0.59	[0.434;0.752]	0.54	[0.25;0.824]
	4 avgs.	0.50	[0.356;0.646]	0.30	[0.057;0.543]
Brainstem	1 avg.	0.56	[0.401;0.71]	0.56	[0.437;0.69]
	2 avgs.	0.63	[0.464;0.79]	0.60	[0.456;0.749]
	4 avgs.	0.48	[0.305;0.659]	0.60	[0.461;0.738]
Overall Image Quality	1 avg.	0.58	[0.395;0.756]	0.48	[0.299;0.656]
	2 avgs.	0.66	[0.483;0.83]	0.57	[0.262;0.874]
	4 avgs.	0.53	[0.391;0.66]	0.46	[0.118;0.802]
Assessment of pathologies	1 avg.	0.51	[0.235;0.775]	0.74	[0.556;0.926]
	2 avgs.	0.50	[0.274;0.734]	0.61	[0.323;0.897]
	4 avgs.	0.66	[0.484;0.83]	0.64	[0.439;0.838]

Avg., average; c-DWI, conventional diffusion-weighted imaging; CI, Confidence interval; DL-DWI, deep learning-based diffusion-weighted imaging; κm, multi-reader kappa

(voxel size 1.6 × 1.6 × 1.6 mm^3) and then normalized to the Montreal Neurological Institute (MNI) brain template (20). This allows access to the associated NMM segmentations (Neuromorphometrics, Inc.) and their application to the diffusion data. The mean and standard deviation of the diffusion parameters were thus determined in the basal ganglia and white matter regions. Furthermore, diffusion data of detected pathologies were manually assessed.

Statistical Analysis

Statistical analysis was performed using SAS 9.4 (SAS Institute, Cary NC). Continuous variables are reported as the mean, standard deviation, minimum, maximum and quartiles. Categorical variables are reported as absolute and relative frequencies. For interrater agreement, the multirater Fleiss kappa ($\varkappa$) was determined. The level of agreement was defined as follows: poor, $\varkappa < 0.21$; fair, $\varkappa = 0.21$–0.40; moderate, $\varkappa = 0.41$–0.60; substantial, $\varkappa = 0.61$–0.80; and almost perfect, $\varkappa = 0.81$–1.0 (21).

For comparison of ordinal data, proportional odds generalized estimating equations (GEE) models were applied. Patients and readers were included as random effects to account for clustered data resulting from multiple-ratings and thus obtaining correct standard errors. An independent working correlation structure was applied since measurements were done independently within clusters. Furthermore, each rater assessed all subjects; hence, the underlying clusters can be described as homogenous. To quantify how the employed MRI acquisition methods compare against each other, odds ratios with corresponding 95%-confidence intervals were calculated.

The continuous pathology and segmentation data were rated by one person, therefore, mixed models for repeated measurements (MMRM) were used. P-values of less than 0.05 were considered statistically significant.

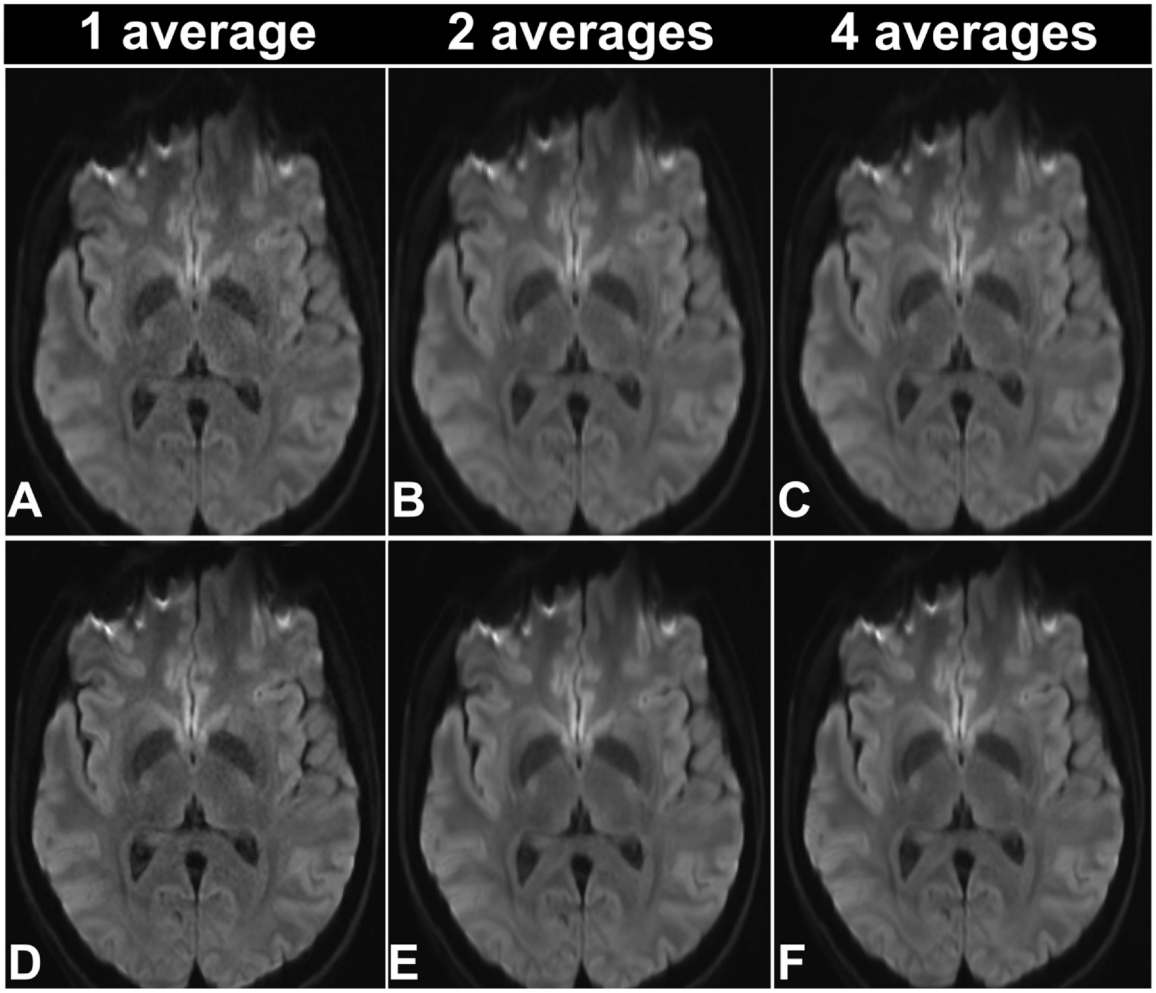

Figure 4. Axial acquisitions of a healthy patient; c-DWI (**a–c**), DL-DWI (**d–f**). C-DWI, conventional diffusion-weighted imaging; DL-DWI, deep learning-based diffusion-weighted imaging.

RESULTS

Description of Patient Data and Findings

Diffusion-weighted images were successfully acquired in all 85 consecutive patients (36 male, 49 female) with a mean age of 55 ranging from 22 to 94 years. Intracranial pathologies were recognized in 35 patients. Patient's characteristics are provided in Table 1.

Subjective Comparison

DL-DWI proved significantly superior for all defined parameters while showing similar results for recognized image artefacts, independently from applied averages (p-value < 0.001). Best results could be shown for DL-DWI with one average revealing excellent overall image quality in 14.5% of cases compared to 0% for c-DWI and in 81% of patients with very good image quality compared to 12.5% for c-DWI, as shown in Figure 3 (Table S3). Thereby, overall image quality (odds ratio [95% confidence interval]: 389.94 [161.55; 941.24]; p-value < 0.001), diagnostic confidence (odds ratio [95% confidence interval]: 412.41 [175.18; 970.89]; p-value < 0.001) and the assessment of pathologies was also significantly superior for DL-DWI with one average (odds ratio [95% confidence interval]: 471.26 [172.17; 1289.94]; p-value < 0.001). By increasing the applied averages, DL-DWI's superiority to conventional MRI becomes less appreciable but is nevertheless still clearly recognizable. It is noteworthy that DL-DWI exhibits a dip in performance when only two averages are considered and gets better with four averages again, slightly better compared to conventional MRI, except for the cerebellum (Table 4). Odds ratios for all defined parameters are displayed in detail in Table 2.

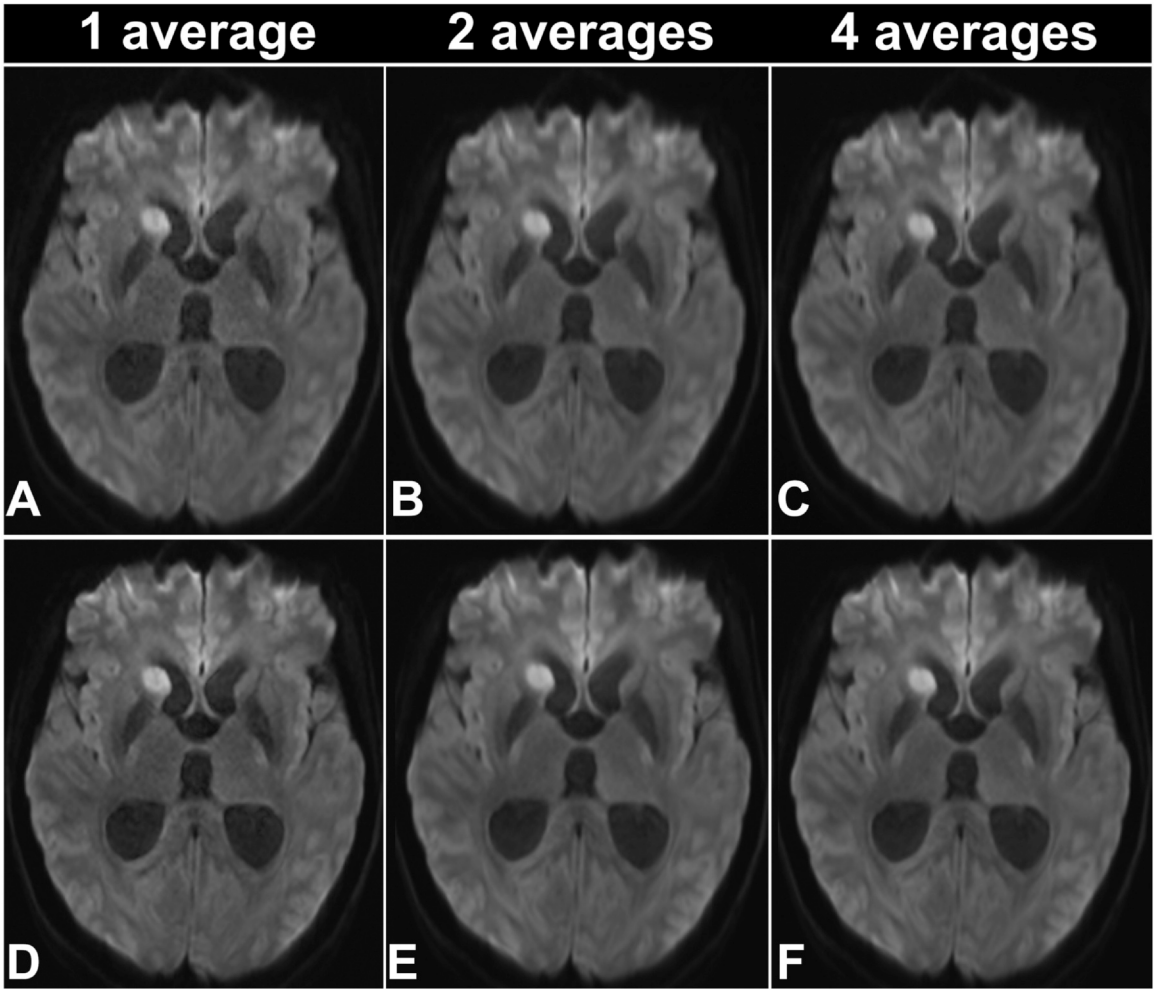

Figure 5. A 51-year-old female patient with a metastasis of breast cancer at the right caput of the nucleus caudatus; c-DWI (**a–c**), DL-DWI (**d–f**). C-DWI, conventional diffusion-weighted imaging; DL-DWI, deep learning-based diffusion-weighted imaging.

DL-DWI did not augment nor create new artefacts, as the Odds ratio did not demonstrate significant differences regardless of applied averages (Table 2). Furthermore, multi-reader inter-rater agreement showed nearly similar results for conventional and deep learning reconstructed images (Table 3).

Figure 4 compares c-DWI vs DL-DWI reconstructions with averages of one, two, and four. Figures 5 and 6 present examples of a 51-year-old female patient with breast cancer and metastasis at the right caput of the nucleus caudatus (Fig 5), and a 61-year-old female patient with subacute ischemia at the left occipital pole after bypass surgery and ECMO (Fig 6). An additional case of a 76-year-old female patient with listeria monocytogenes infection of the brain and concomitant ventriculitis is presented in Figure 7.

Inter-rater Fleiss' Kappa demonstrated moderate to substantial agreement for virtually all defined parameters, with good accordance, particularly for the assessment of pathologies ($\varkappa$ = 0.74). For the detailed results of multi-reader inter-rater agreement for DWI refer to Table 3.

(Semi-)Quantitative Image Analysis

The signal values of the diffusion parameters of the basal ganglia, the white matter of the precentral region, and detected pathologies did not demonstrate significant differences between different averages and techniques. A detailed comparison of absolute DWI and ADC values for different averages and techniques is given in Table Table 4.

DISCUSSION

This study aimed at testing the clinical feasibility of a novel deep learning-enhanced DWI Sequence and demonstrating its advantages by comparing it to conventional diffusion-weighted

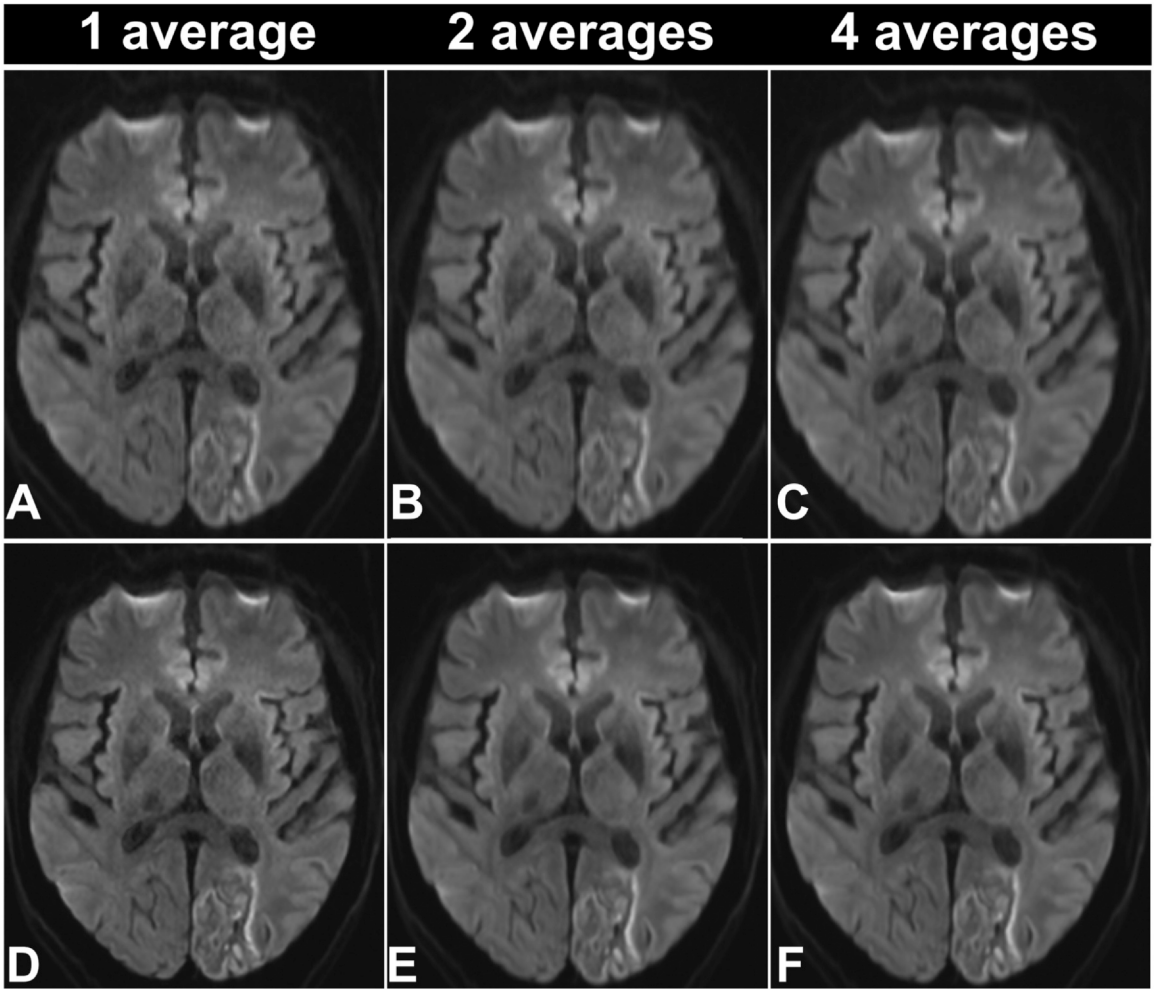

Figure 6. A 61-year-old female patient with subacute ischemia at the left occipital pole after bypass surgery and ECMO. Note the superior image quality of DL-DWI; c-DWI (**a–c**), DL-DWI (**d–f**). C-DWI, conventional diffusion-weighted imaging; DL-DWI, deep learning-based diffusion-weighted imaging.

imaging. Our results show that super resolution DL-DWI has the potential to markedly shorten acquisition times without compromising image quality. Image quality was rated superior in DL-DWI scans compared to conventional reconstructions with even longer acquisition times for all defined parameters. With a total acquisition time of 50 s, DL-DWI demonstrated even superior image quality and diagnostic confidence compared to c-DWI, which had four averages and a total acquisition time of 119 s. Furthermore, we were able to show that deep learning-based reconstruction has no impact on apparent diffusion coefficient quantitation, as demonstrated in previous publications (22). We could also demonstrate the technique's robustness, as DL-DWI did not augment or create new artefacts. To the best of our knowledge, this is the first study to present and evaluate this novel DL-DWI algorithm at 3 Tesla for brain MRI.

Super resolution is a technique that can enhance image sharpness and reduce blurring without altering the acquisition parameters of conventional imaging techniques. This can improve the overall quality of the image. Additionally, this approach can be used simultaneously with denoising techniques to further enhance the image quality (23–25).

In general, high-resolution DWI is in crucial demand as it offers the potential to gain an in-depth comprehension of in-vivo tissue microstructure. Thereby, multi-b-value diffusion MRI methods can provide valuable insights into the tissue microstructure by pseudo-diffusion and non-Gaussian components of water molecule diffusion, especially in structurally complex tissues (26). Up to this point, single-shot echo-planar imaging (EPI) has been a routinely

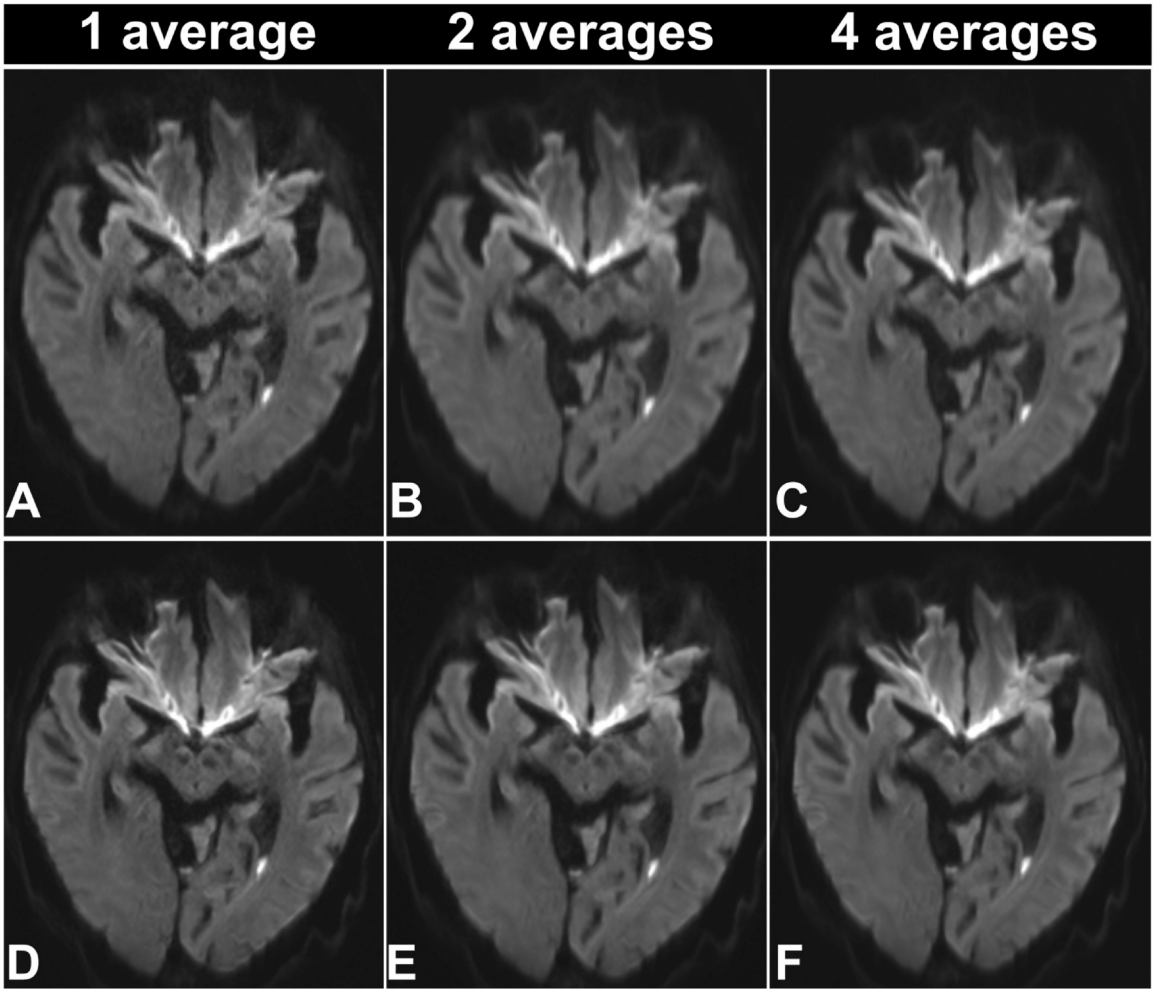

Figure 7. A 76-year-old female patient with listeria monocytogenes infection of the brain and concomitant ventriculitis c-DWI (**a–c**), DL-DWI (**d–f**). C-DWI, conventional diffusion-weighted imaging; DL-DWI, deep learning-based diffusion-weighted imaging.

used technique. However, it is essential to understand that this acquisition method has several limitations, such as T2 * blurring, susceptibility artefacts, and background noise, which can impair diagnostic accuracy. Scanning time has to be increased (e.g., by applying additional averages) to improve image quality and to allow for high spatial resolution with conventional methods (27). With a steady increase in medical examinations and financial pressure on healthcare providers, employing strategies to improve image quality without delaying clinical workflow is crucial (28,29).

Up to date, in order to generate fast DWI, conventional acceleration techniques, such as SMS, ssEPI and GRAPPA reconstruction, are most often used. Using these techniques, there is always a trade-off between image quality and the benefit of rapid image acquisition in terms of restless patients or emergency settings (14,30). Integrating deep-learning enhanced MRI into clinical routine can lead to expedited diagnostic processes with markedly reduced examination times while maintaining the standard of diagnostic image quality (13,14,31,32). As highlighted in this study, novel methods of deep learning-based MRI reconstruction can help establish high-resolution DWI in the clinical routine and significantly improve image quality when highly accelerated images are required.

This study has limitations. The generalizability of our results is hampered as this is a single-center study. In addition, we did not evaluate the diagnostic accuracy for particular diseases. Further studies with larger samples and homogeneous pathologies are therefore needed.

TABLE 4. Detailed Comparison of Absolute ADC and DWI Values for c-DWI and DL-DWI

Parameter			Estimate	SE	95%-CI	p-value
ADC-Value Pathology	c-DWI	1 avg.	1312.6	167.04	985.23;1640.01	
		2 avgs.	-52.82	59.98	-170.38; 64.74	0.378
		4 avgs.	-5.50	13.87	-32.68; 21.68	0.692
	DL-DWI	1 avg.	5.85	7.45	-8.74; 20.45	0.432
		2 avgs.	0.29	11.76	-22.76; 23.35	0.980
		4 avgs.	3.21	15.14	-26.47; 32.88	0.832
DWI-value pathology	c-DWI	1 avg.	228.74	26.20	177.39; 280.08	
		2 avgs.	-1.35	2.58	-6.41; 3.70	0.600
		4 avgs.	-2.94	4.37	-11.50; 5.62	0.501
	DL-DWI	1 avg.	-1.38	4.04	-9.30; 6.54	0.732
		2 avgs.	-0.74	3.82	-8.22; 6.75	0.847
		4 avgs.	0.85	3.25	-5.53; 7.23	0.793
ADC central region	c-DWI	1 avg.	868.92	7.47	854.06; 883.77	
		2 avgs.	-0.25	10.56	-21.01; 20.52	0.981
		4 avgs.	4.44	10.56	-16.33; 25.20	0.675
		1 avg.	14.31	10.56	-6.46; 35.07	0.176
		2 avgs.	13.92	10.56	-6.85; 34.68	0.188
		4 avgs.	19.21	10.56	-1.55; 39.98	0.070
DWI central region	c-DWI	1 avg.	148.38	4.08	140.26; 156.49	
		2 avgs.	-0.07	5.77	-11.42; 11.28	0.990
		4 avgs.	-0.86	5.77	-12.21; 10.49	0.882
	DL-MRI	1 avg.	0.95	5.77	-10.39; 12.30	0.869
		2 avgs.	0.65	5.77	-10.70; 11.99	0.911
		4 avgs.	9.38	5.77	-1.97; 20.72	0.105
ADC basal ganglia	c-DWI	1 avg.	1155.4	32.62	1090.58;1220.3	
		2 avgs.	-2.55	46.13	-93.23; 88.12	0.956
		4 avgs.	-0.64	46.13	-91.31; 90.04	0.989
	DL-MRI	1 avg.	37.74	46.13	-52.93; 128.42	0.414
		2 avgs.	36.91	46.13	-53.77; 127.58	0.424
		4 avgs.	41.44	46.13	-49.24; 132.11	0.370
DWI basal ganglia	c-DWI	1 avg.	125.04	6.46	112.20; 137.98	
		2 avgs.	-0.07	9.13	-18.02; 17.87	0.994
		4 avgs.	-0.66	9.13	-18.60; 17.29	0.943
	DL-MRI	1 avg.	-0.86	9.13	-18.80; 17.09	0.925
		2 avgs.	-1.27	9.13	-19.22; 16.67	0.889
		4 avgs.	12.46	9.13	-5.49; 30.40	0.173

All statistics based on GEE. Patients were included as random effects. p-Value: based on score test with the nullhypothesis of effect estimates being zero; assessment was performed only by reader 1; ADC, apparent diffusion coefficient; c-DWI, conventional diffusion-weighted imaging; DL-DWI, deep learning-based diffusion-weighted imaging.

CONCLUSION

Ultra-fast diffusion-weighted imaging with super resolution is feasible, resulting in highly accelerated brain imaging while increasing diagnostic image quality. This technique has the potential to further strengthen the role of MRI, especially in neurological emergencies.

FUNDING

The authors declare that no funds or grants were received during the preparation of this manuscript. Thomas Benkert is employed by Siemens and provided work-in-progress sequences and writing assistance for the paragraph "deep learning reconstruction".

DECLARATION OF COMPETING INTEREST

The authors declare the following financial interests/personal relationships which may be considered as potential competing interests: Sebastian Altmann reports writing assistance was provided by Siemens Healthineers AG, Erlangen, Germany. Thomas Benkert reports a relationship with Siemens Healthineers AG, Erlangen, Germany that includes: employment. Thomas Benkert has patent pending to Siemens Healthineers AG. If there are other authors, they

declare that they have no known competing financial interests or personal relationships that could have appeared to influence the work reported in this paper.

APPENDIX A. SUPPORTING INFORMATION

Supplementary data associated with this article can be found in the online version at doi:10.1016/j.acra.2024.02.049.

REFERENCES

1. Baliyan V, Das CJ, Sharma R, et al. Diffusion weighted imaging: technique and applications. World J Radiol 2016; 8(9):785–798.
2. Drake-Perez M, Boto J, Fitsiori A, et al. Clinical applications of diffusion weighted imaging in neuroradiology. Insights Imaging 2018; 9(4):535–547.
3. Chalela JA, Kidwell CS, Nentwich LM, et al. Magnetic resonance imaging and computed tomography in emergency assessment of patients with suspected acute stroke: a prospective comparison. Lancet 2007; 369(9558):293–298.
4. Mintorovitch J, Moseley ME, Chileuitt L, et al. Comparison of diffusion- and T2-weighted MRI for the early detection of cerebral ischemia and reperfusion in rats. Magn Reson Med 1991; 18(1):39–50.
5. Moseley ME, Cohen Y, Mintorovitch J, et al. Early detection of regional cerebral ischemia in cats: comparison of diffusion- and T2-weighted MRI and spectroscopy. Magn Reson Med 1990; 14(2):330–346.
6. Venkatesan R, Lin W, Gurleyik K, et al. Absolute measurements of water content using magnetic resonance imaging: preliminary findings in an in vivo focal ischemic rat model. Magn Reson Med 2000; 43(1):146–150.
7. Jezzard P, Balaban RS. Correction for geometric distortion in echo planar images from B0 field variations. Magn Reson Med 1995; 34(1):65–73.
8. Andersson JL, Skare S, Ashburner J. How to correct susceptibility distortions in spin-echo echo-planar images: application to diffusion tensor imaging. Neuroimage 2003; 20(2):870–888.
9. Xiong Y, Li G, Dai E, et al. Distortion correction for high-resolution single-shot EPI DTI using a modified field-mapping method. NMR Biomed 2019; 32(9):e4124.
10. Thian YL, Xie W, Porter DA, et al. Readout-segmented echo-planar imaging for diffusion-weighted imaging in the pelvis at 3T-A feasibility study. Acad Radiol 2014; 21(4):531–537.
11. Viallon M, Cuvinciuc V, Delattre B, et al. Erratum to: state-of-the-art MRI techniques in neuroradiology: principles, pitfalls, and clinical applications. Neuroradiology 2015; 57(10):1075.
12. Xie D, Li Y, Yang H, et al. Denoising arterial spin labeling perfusion MRI with deep machine learning. Magn Reson Imaging 2020; 68:95–105.
13. Gassenmaier S, Afat S, Nickel MD, et al. Accelerated T2-weighted TSE imaging of the prostate using deep learning image reconstruction: a prospective comparison with standard T2-weighted TSE imaging. Cancers (Basel) 2021; 13(14):3593. https://doi.org/10.3390/cancers13143593. PMID: 34298806; PMCID: PMC8303682.
14. Altmann S, Abello Mercado MA, Brockstedt L, et al. Ultrafast brain MRI protocol at 1.5 T using deep learning and multi-shot EPI. Acad Radiol 2023; 30(12):2988–2998. https://doi.org/10.1016/j.acra.2023.04.019. Epub 2023 May 19. PMID: 37211480.
15. Koktzoglou I, Huang R, Ankenbrandt WJ, et al. Super-resolution head and neck MRA using deep machine learning. Magn Reson Med 2021; 86(1):335–345.
16. Gassenmaier S, Afat S, Nickel D, et al. Deep learning-accelerated T2-weighted imaging of the prostate: Reduction of acquisition time and improvement of image quality. Eur J Radiol 2021; 137:109600.
17. Hammernik K, Klatzer T, Kobler E, et al. Learning a variational network for reconstruction of accelerated MRI data. Magn Reson Med 2018; 79(6):3055–3071.
18. Tao W, Pan Z, Wu G, et al. The strength of Nesterov's extrapolation in the individual convergence of nonsmooth optimization. IEEE Trans Neural Netw Learn Syst 2020; 31(7):2557–2568.
19. W. Shi J. Caballero F. Huszár et al. Real-time single image and video super-resolution using an efficient sub-pixel convolutional neural network Proceedings of the IEEE conference on computer vision and pattern recognition 2016 1874 1883.
20. Collins DL, Neelin P, Peters TM, et al. Automatic 3D intersubject registration of MR volumetric data in standardized Talairach space. J Comput Assist Tomogr 1994; 18(2):192–205.
21. Landis JR, Koch GG. The measurement of observer agreement for categorical data. Biometrics 1977; 33(1):159–174. PMID: 843571.
22. Ueda T, Ohno Y, Yamamoto K, et al. Deep learning reconstruction of diffusion-weighted MRI improves image quality for prostatic imaging. Radiology 2022; 303(2):373–381.
23. Afat S, Wessling D, Afat C, et al. Analysis of a deep learning-based superresolution algorithm tailored to partial fourier gradient echo sequences of the abdomen at 1.5 T: reduction of breath-hold time and improvement of image quality. Invest Radiol 2022; 57(3):157–162.
24. Plenge E, Poot DH, Bernsen M, et al. Super-resolution methods in MRI: can they improve the trade-off between resolution, signal-to-noise ratio, and acquisition time? Magn Reson Med 2012; 68(6):1983–1993.
25. Wessling D, Herrmann J, Afat S, et al. Application of a deep learning algorithm for combined super-resolution and partial fourier reconstruction including time reduction in T1-weighted precontrast and postcontrast gradient echo imaging of abdominopelvic MR imaging. Diagnostics (Basel) 2022; 12(10):2370. https://doi.org/10.3390/diagnostics12102370. PMID: 36292057; PMCID: PMC9600324.
26. Koprivova T, Kerkovsky M, Juza T, et al. Possibilities of using multi-b-value diffusion magnetic resonance imaging for classification of brain lesions. Acad Radiol 2024; 31(1):261–272.
27. Coll B., Morel J.-M. A non-local algorithm for image denoising 2005.
28. McBee MP, Awan OA, Colucci AT, et al. Deep learning in radiology. Acad Radiol 2018; 25(11):1472–1480.
29. Saba L, Biswas M, Kuppili V, et al. The present and future of deep learning in radiology. Eur J Radiol 2019; 114:14–24.
30. Ha JY, Baek HJ, Ryu KH, et al. One-minute ultrafast brain MRI with full basic sequences: can it be a promising way forward for pediatric neuroimaging? Am J Roentgenol 2020; 215(1):198–205.
31. Bash S, Wang L, Airriess C, et al. Deep learning enables 60% accelerated volumetric brain MRI while preserving quantitative performance: a prospective, multicenter, multireader trial. Am J Neuroradiol 2021; 42(12):2130–2137.
32. Tajima T, Akai H, Yasaka K, et al. Usefulness of deep learning-based noise reduction for 1.5 T MRI brain images. Clin Radiol 2023; 78(1):e13–e21.